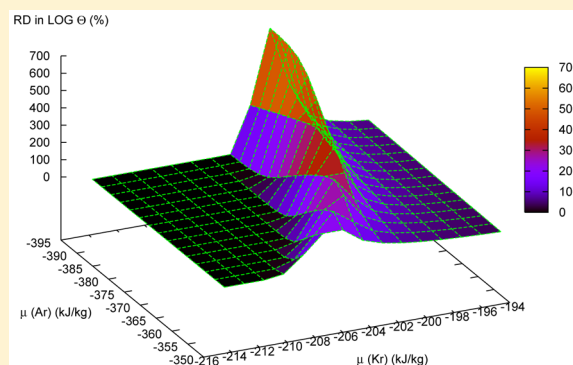


Many-Body Effects on the Thermodynamics of Fluids, Mixtures, and Nanoconfined Fluids

Caroline Desgranges and Jerome Delhommelle*

Department of Chemistry, University of North Dakota, Grand Forks, North Dakota 58202, United States

ABSTRACT: Using expanded Wang–Landau simulations, we show that taking into account the many-body interactions results in sharp changes in the grand-canonical partition functions of single-component systems, binary mixtures, and nanoconfined fluids. The many-body contribution, modeled with a 3-body Axilrod–Teller–Muto term, results in shifts toward higher chemical potentials of the phase transitions from low-density phases to high-density phases and accounts for deviations of more than, e.g., 20% of the value of the partition function for a single-component liquid. Using the statistical mechanics formalism, we analyze how this contribution has a strong impact on some properties (e.g., pressure, coexisting densities, and enthalpy) and a moderate impact on others (e.g., Gibbs or Helmholtz free energies). We also characterize the effect of the 3-body terms on adsorption isotherms and adsorption thermodynamic properties, thereby providing a full picture of the effect of the 3-body contribution on the thermodynamics of nanoconfined fluids.



1. INTRODUCTION

Molecular simulation methods have become increasingly accurate at predicting a wide range of properties in fields as diverse as chemistry, biology, physics, and materials science. The accuracy of the simulation results hinges on the existence of high-performance algorithms and of high-quality force fields, leading to an accurate modeling of the properties of the compounds under study. A large number of the most popular and widely used force fields^{1–13} rely on the use of effective two-body potentials, such as, e.g., the Lennard–Jones form, and have been parametrized by fitting large experimental data sets. The empirical nature of the parameters may, however, limit the accuracy of the force fields for systems or conditions outside of those covered in the data set. In such cases, the development of many-body potentials, based on *ab initio* calculations, provides an alternative approach and has been the focus of intense research in recent years. There are several possible routes to design and parametrize a many-body force field. A possible choice consists of supplementing a high-quality *ab initio* pair potential with a 3-body Axilrod–Teller–Muto term^{14,15} to model the *ab initio* 3-body exchange and dispersion interactions.^{16,17} Many-body potentials are now being extensively developed for a wide range of systems,^{18–30} including molecular systems,^{31–37} such as, e.g., water,^{38–40} alkanes or amines,^{41,42} and even peptides.⁴³ Many-body force fields have been shown to lead to very promising results, e.g., for condensed-phase properties^{19,44–48} or phase equilibria properties.^{27,49–54} Much less is known, however, on the impact of 3-body interactions on other thermodynamic properties, such as, e.g., the Gibbs free energy and the entropy. Furthermore, few studies have focused on nanoconfined systems,⁵⁵ and the impact of 3-body interactions on the adsorption properties, as

well on the selectivity for the adsorption of mixtures, remains unclear. Therefore, a full picture of the impact of the many-body interaction terms on the statistical mechanics of fluids, fluid mixtures, and nanoconfined fluids, and on their derived thermodynamic properties, has yet to emerge.

Conventional Monte Carlo and molecular dynamics methods⁵⁶ are very efficient at calculating equilibrium properties for a specific set of conditions, generally given as input parameters for the simulation. On the other hand, advanced non-Boltzmann sampling schemes, such as the Wang–Landau method,^{57,58} have the advantage of allowing all states accessible to the system to be thoroughly explored. Furthermore, this method gives a full picture of the statistical mechanics of the system, providing, e.g., the partition function for the corresponding statistical ensemble.^{59–63} Having an accurate estimate for the partition function is extremely useful, as all thermodynamic properties of the system can be readily calculated from the partition function through the formalism of statistical thermodynamics. In this work, we determine the contribution made by the 3-body interactions to the grand-canonical partition function of systems under a wide range of conditions and settings. For this purpose, we use the recently developed expanded Wang–Landau (EWL) simulation method^{59,64,65} to calculate the grand-canonical partition functions of single-component systems, binary mixtures, and nanoconfined systems of noble gases, modeled by a combination of a 2-body *ab initio* pair potential and a 3-body Axilrod–Teller term. For a single-component system with a chemical potential μ , a volume

Received: July 21, 2015

Published: September 30, 2015

Table 1. Parameters for the Two-Body Interatomic Interactions^a

	A/E_h	α/a_0^{-1}	β/a_0^{-2}	b/a_0^{-1}	$C_6/(E_h a_0^6)$	$C_8/(E_h a_0^8)$	$C_{10}/(E_h a_0^{10})$
Ar–Ar	56.21	1.31938	−0.050	1.70	60.98	1941.02	62960.00
Kr–Kr	109.66	1.32512	−0.0404	1.40	120.14	3565.02	364467.00
Ar–Kr	112.08	1.42241	−0.040	1.50	94.08	2452.27	93790.30

^a $E_h = 4.3597 \times 10^{-18}$ J.

V , and a temperature T , the grand-canonical partition function is given by

$$\Theta(\mu, V, T) = \sum_{N=0} Q(N, V, T) \exp(\beta\mu N) \quad (1)$$

The goal of this work is 2-fold: First, we determine the impact of the 3-body interactions on $\Theta(\mu, V, T)$ of noble gases and their mixtures, both as bulk phases and under nanoconfinement. We show that including the 3-body contribution leads to shifts toward higher chemical potentials for the phase transitions and thus results in sharp changes in $\Theta(\mu, V, T)$ for a given value of the chemical potential μ . We analyze this result in terms of the relative contribution from the two terms involved in the sum in eq 1, i.e., the μ -dependent weighting factor $\exp(\beta\mu N)$ and the $Q(N, V, T)$ function, which does not depend on μ . Second, we relate these sharp changes in the partition function to the impact of the 3-body term on the prediction of thermodynamic properties. To this end, we consider a wide range of thermodynamic properties, including the Gibbs free energy, entropy, and vapor–liquid equilibria of bulk fluids and mixtures. In the case of nanoconfined systems, we analyze the 3-body contribution to excess thermodynamic properties, adsorption isotherms, and, for nanoconfined mixtures, pore selectivity.

The article is organized as follows: We first present the 2-body potential, together with the 3-body Axilrod–Teller term, used to model Ar and Kr in this work. We discuss how we apply the EWL approach to determine the partition functions of single-component systems, binary mixtures, and nanoconfined systems. Then, for each system, we analyze the impact of the 3-body contribution on the grand-canonical partition function, elucidate the role played by the μ -dependent terms, and characterize the effect of the 3-body term on the thermodynamic properties of fluids and fluid mixtures, in the bulk or under nanoconfinement. We finally draw the main conclusions from this work in the last section.

2. TWO- AND THREE-BODY INTERACTION POTENTIALS

The models used in this work are based on the *ab initio* potentials developed by Deiters and co-workers.^{49,50,66} The *ab initio* 2-body potential is calculated using the CCSD(T) level of theory and several correlation consistent basis sets.^{66,67} The results obtained with the different correlation consistent basis sets^{49,50} are then extrapolated toward the basis set limit for the interaction energies using the $1/X^3$ method. For the Ar–Ar potential, the aug-cc-pVQZ and aug-cc-pVSZ basis sets were used, with the extrapolation results being referred to as *av45z* in the work by Nasrabad et al.¹⁸ For the Kr–Kr interaction, the aug-cc-pVTZ and aug-cc-pVQZ basis sets were used, with the extrapolation results termed *av34z*. Similarly, for Ar–Kr interactions, the aug-cc-pVTZ and aug-cc-pVQZ basis sets were used, and the extrapolation results were termed *av34z*. The quantum mechanical results were then fitted to the functional form of Korona et al.⁶⁸ This gives the 2-body (2B)

potential (which is taken to be, in this work, an *ab initio* pair potential and not an effective pair potential) with the following functional form for the interaction between two atoms i and j

$$\phi_{2B}(r_{ij}) = A_{ij} \exp[-\alpha_{ij}r_{ij} + \beta_{ij}r_{ij}^2] + \sum_{n=3}^5 f_{2n}(r_{ij}, b_{ij}) \frac{C_{2n,ij}}{r_{ij}^{2n}} \quad (2)$$

where r_{ij} is the distance between the two atoms i and j and A_{ij} , α_{ij} , β_{ij} , b_{ij} , and $C_{2n,ij}$ are the potential parameters given in Table 1. The f_{2n} terms are the damping functions of Tang and Toennies⁶⁹

$$f_{2n}(r_{ij}, b_{ij}) = 1 - \exp[-b_{ij}r_{ij}] + \sum_{k=0}^{2n} \frac{(b_{ij}r_{ij})^k}{k!} \quad (3)$$

The 3-body potential (3B) is obtained by adding an Axilrod–Teller–Muto (ATM) triple-dipole potential^{14,15} to the *ab initio* pair potential. We use the following functional form for the Axilrod–Teller potential

$$\phi_{AT} = \sqrt[3]{\nu_i \nu_j \nu_k} \left(\frac{1 + 3 \cos \alpha \cos \beta \cos \gamma}{r_{ij}^3 r_{ik}^3 r_{jk}^3} \right) \quad (4)$$

where r_{ij} , r_{ik} , and r_{jk} are the distances between pairs of atoms within the triplet (i, j, k) and α , β , and γ are the angles of the triangle formed by the three atoms i , j , and k . ν_i , ν_j , and ν_k are the Axilrod–Teller constants associated with each atom^{49–51} ($\nu_{Ar} = 7.32 \times 10^{-18}$ J·Å⁹ and $\nu_{Kr} = 2.20 \times 10^{-17}$ J·Å⁹). We add that the ATM approach relies on fixed polarizabilities to evaluate many-body effects. Recent calculations on carbon nanostructures, based on solving the self-consistent screening equation for systems modeled with quantum harmonic oscillators coupled through a dipole–dipole potential, have highlighted the system size dependence of the van der Waals coefficient of carbon atoms.^{70,71}

3. EXPANDED WANG–LANDAU SIMULATIONS

3.1. Theoretical Framework. We recently proposed the expanded Wang–Landau (EWL) method^{59,64,65} to determine the numerical value of the grand-canonical partition function of atomic and molecular fluids. We briefly discuss in this section the theoretical background underlying this type of simulation.

The EWL approach is a Monte Carlo (MC) simulation that builds upon the well-known Wang–Landau (WL) sampling technique^{57,58,60–63,72–77} to evaluate dynamically the value of the partition function of the system. The accuracy of the iterative process relies on an extensive sampling of the ensemble, e.g., of all possible numbers of atoms N in the case of the grand-canonical ensemble (μ, V, T) .^{59,64,65} The usual grand-canonical MC scheme relies on insertion/deletion steps to sample different N values. However, the acceptance rates for the insertion/deletion steps decrease with density and becomes extremely low for high-density liquids. This implies that the usual grand-canonical MC scheme cannot be used to obtain

accurate estimates for the partition function. To solve this issue, we use an approach based on an expanded ensemble.^{78–86} In this method, the system contains N atoms and a fractional atom at stage l , with l being an integer such that $0 \leq l < M$, where M is the number of stages into which the insertion/deletion of a full atom is divided. When $l = 0$, the fractional atom is void and the system is exactly equivalent to a system with N atoms. The fractional atom interacts with the full atoms through a coupling parameter ξ_l (see the next section for additional technical details) and can grow (or shrink). Different N values are thus sampled through changes in the l value of the fractional atom. For instance, whenever l is increased beyond M , the fractional atom becomes a full atom and a new fractional atom at stage $l - M$ is created.

In this work, we study the effect of the many-body interactions on the thermodynamics of the fluid phases of a pure substance (one-component system) and of binary mixtures (two-component systems). For a one-component system, the EWL method uses a self-consistent scheme to determine the numerical value of the functions $Q(N, V, T, l)$ for all (N, l) values, defined as⁵⁹

$$Q(N, V, T, l) = \frac{V^{N+1}}{N! \Lambda^{3(N+1)}} \int \exp(-U(\Gamma)/k_B T) d\Gamma$$

$$(0 < l < M)$$

$$Q(N, V, T, l = 0) = \frac{V^N}{N! \Lambda^{3N}} \int \exp(-U(\Gamma)/k_B T) d\Gamma$$

(5)

in which Λ is the de Broglie wavelength and Γ denotes a specific configuration of a system of N atoms.

The grand-canonical partition function $\Theta(\mu, V, T)$ for a given chemical potential μ can then be calculated from all $Q(N, V, T, l = 0)$ (denoted $Q(N, V, T)$ hereafter) as

$$\Theta(\mu, V, T) = \sum_N Q(N, V, T) \exp(\beta \mu N)$$

(6)

For a two-components system, the output from the EWL simulations⁶⁵ are $Q(N_1, N_2, V, T, l_1, l_2)$ and the grand-canonical partition function $\Theta(\mu_1, \mu_2, V, T)$ can be obtained from the values of $Q(N_1, N_2, V, T, l_1 = 0, l_2 = 0)$ (denoted $Q(N_1, N_2, V, T)$ hereafter) as

$$\Theta(\mu_1, \mu_2, V, T) = \sum_{N_1} \sum_{N_2} Q(N_1, N_2, V, T) \exp(\beta(\mu_1 N_1 + \mu_2 N_2))$$

(7)

3.2. Simulation Details. For each of the systems studied in this work, we carry out two series of EWL simulations (one with the 2B potential and one with the 3B potential) in order to assess the effect of the contribution of the 3-body interactions. The EWL MC steps consist of either the translation of a single atom (75% of the MC steps) or of a change in (N, l) (25% of the MC steps). To ensure a smooth transition when the fractional atom grows to become full or shrinks to become void, the potential for the interaction between a fractional atom and a full atom has a similar form as the potential for the interaction between full atoms. We start by introducing the coupling parameter ξ_l for a fractional atom at stage l , as $\xi_l = l/M$. Following the scaling strategy used for the Lennard-Jones potential,^{39,64,65} we define the interaction between a fractional atom and a full atom as given by

$$\phi(r) = \frac{1}{\xi_l^{1/3}} \left(A \exp \left[-\frac{\alpha}{\xi_l^{1/4}} r + \frac{\beta}{\xi_l^{1/2}} r^2 \right] + \sum_{n=3}^5 \xi_l^{n/2} f_{2n}(r, b) \frac{C_{2n}}{r^{2n}} \right)$$

(8)

We compare in Figure 1 the interaction potential between Ar atoms to the interaction between a fractional atom and a full Ar

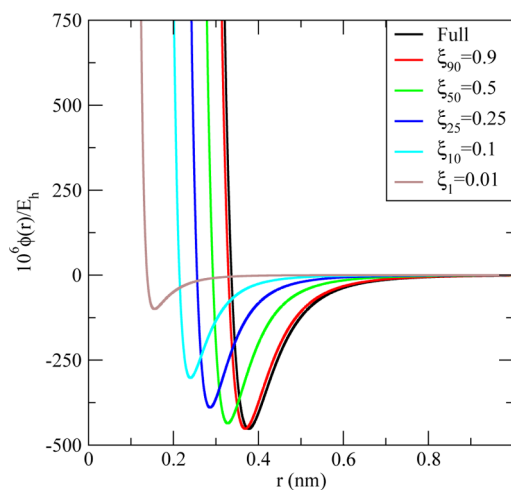


Figure 1. Argon: Interaction between the fractional atom with a full atom for various values of the coupling parameter $\xi_l = l/M$ ($M = 100$). The potential for the interaction between two full Ar atoms is also shown.

atom for different values of the coupling parameter ξ_l . Figure 1 shows that, for a small ξ_l (see, e.g., the value of 0.01 for the coupling parameter), the exclusion diameter is fairly small, which facilitates the creation of new atoms in the system. Furthermore, we see that the gradual increase in the value of ξ_l results in a smooth transition from a fractional atom to a full atom (see, e.g., the value of 0.9 for the coupling parameter). We use the same functional form to model the interaction between a fractional atom and a full atom for both the 2B and 3B potentials.

The other technical details regarding the Wang–Landau scheme are exactly the same as previously described,^{59,64,65} with the final value of the convergence factor set to $f = 10^{-8}$ and a number of intermediate stages set to $M = 100$. In simulations of single-component and binary mixtures, EWL simulations are run on systems containing up to a total of 200 atoms, with periodic boundary conditions applied in the three directions, and a spherical truncation was applied to the calculations of the interactions, with the usual tail corrections applied beyond the cutoff set to half the boxlength for the 2-body contributions⁵⁶ and beyond a cutoff set to a quarter of the boxlength for the 3-body contributions.⁵⁰

For nanoconfined systems, we consider a slit pore geometry and use a popular model for the two confining walls,^{87,88} known as the Steele 9-3 potential. The fluid is confined between two planar walls (with dimensions of $25 \times 25 \text{ \AA}^2$) separated by a distance of 12 \AA along the z -axis. The effective interaction between the atoms of the fluid with the top wall (located at $S_z/2 = 6 \text{ \AA}$ along the z -axis) is given by

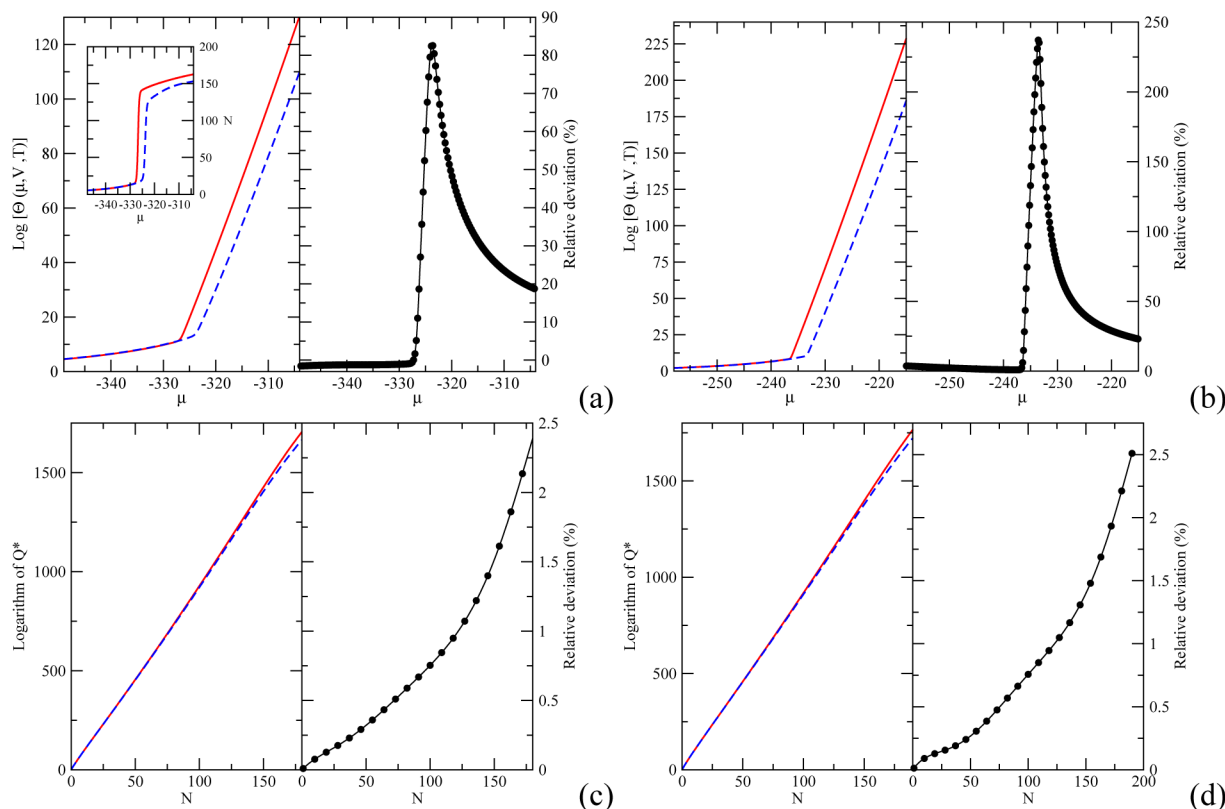


Figure 2. (a) Argon at $T = 140$ K: (left) logarithm of $\Theta(\mu, V, T)$ against the chemical potential μ in kJ/kg (red solid line, 2B potential; blue dashed line, 3B potential), (inset) number of atoms N against the chemical potential μ , and (right) relative deviation between the 2B and 3B results. (b) Krypton at $T = 180$ K: (left) logarithm of $\Theta(\mu, V, T)$ (same legend as in (a)) and (right) relative deviation between the 2B and 3B results. (c) Argon at $T = 140$ K: (left) logarithm of $Q^*(N, V, T) = \Lambda_{\text{Ar}}^{3N} Q(N, V, T)$ against the number of Ar atoms (same legend as in (a)) and (right) relative deviation between the 2B and 3B results. (d) Krypton at $T = 180$ K: (left) logarithm of $Q^*(N, V, T) = \Lambda_{\text{Kr}}^{3N} Q(N, V, T)$ against the number of Kr atoms (same legend as in (a)) and (right) relative deviation between the 2B and 3B results.

$$\phi_{\text{wf}}^t(z) = \frac{2\pi\rho_w\sigma_{\text{wf}}^3\epsilon_{\text{wf}}}{3} \left[\frac{2}{15} \left(\frac{\sigma_{\text{wf}}}{S_z/2 - z} \right)^9 - \left(\frac{\sigma_{\text{wf}}}{S_z/2 - z} \right)^3 \right] \quad (9)$$

whereas the interaction with the bottom wall (located at $-S_z/2 = -6$ Å along the z -axis) is

$$\phi_{\text{wf}}^b(z) = \frac{2\pi\rho_w\sigma_{\text{wf}}^3\epsilon_{\text{wf}}}{3} \left[\frac{2}{15} \left(\frac{\sigma_{\text{wf}}}{S_z/2 + z} \right)^9 - \left(\frac{\sigma_{\text{wf}}}{S_z/2 + z} \right)^3 \right] \quad (10)$$

The parameters for the number density for the wall ($\rho_w = 0.097$ atoms/Å³) and for the effective wall–fluid parameters σ_{wf} and ϵ_{wf} are taken from previous work.^{89–91} In the case of argon, the wall–fluid parameters are $\sigma_{\text{w-Ar}} = 2.8$ Å and $\epsilon_{\text{w-Ar}}/k_B = 107.32$ K, whereas for krypton, we have $\sigma_{\text{w-Kr}} = 2.92$ Å and $\epsilon_{\text{w-Kr}}/k_B = 126.43$ K. Periodic boundary conditions are applied in two directions only, i.e., along the x and y axes, and no tail corrections were applied beyond the cutoff radii (set to the same value as for bulk phases).

4. RESULTS AND DISCUSSION

4.1. Single-Component Fluids. We begin by analyzing the results obtained for single-component fluids. We present the EWL results for the grand-canonical partition function $\Theta(\mu, V, T)$, obtained either with the 2B or 3B potential, for Ar in Figure 2a and for Kr in Figure 2b. While the 2B and 3B

results are in excellent agreement for low μ values (corresponding to low-density systems), Figure 2 shows that the two functions start to depart significantly from each other as μ increases. For instance, in the case of Ar, the 2B $\Theta(\mu, V, T)$ increases steeply when $\mu > -327$ kJ/kg, whereas the 3B $\Theta(\mu, V, T)$ increases for larger chemical potentials ($\mu > -323.5$ kJ/kg). The steep increase in $\Theta(\mu, V, T)$ is associated with the phase change from a low-density phase (vapor) to a high-density phase (liquid). This means that taking into account the 3-body interaction shifts the transition to higher μ values, as shown by the peak observed in the relative deviation (defined as $\text{RD}(\%) = 100 \times (\log \Theta_{2B} / \log \Theta_{3B} - 1)$) between the 2B and 3B results (see the right panels of Figure 2a,b). After both the 2B and 3B grand-canonical partition functions continue to depart significantly from each other, e.g., by 48.6% at $\mu = -320$ kJ/kg and by 23.5% at $\mu = -310$ kJ/kg. Similar results are observed for Kr (see Figure 2b).

As shown in eq 6, $\Theta(\mu, V, T)$ is calculated by summing up the functions $Q(N, V, T)$, weighted by the factor $\exp[\beta\mu N]$. To better understand the source of the large deviations observed for $\Theta(\mu, V, T)$, it is, therefore, useful to compare the $Q(N, V, T)$ obtained with the 2B and 3B potentials. We show in Figure 2c,d the 2B and 3B $Q(N, V, T)$ obtained with the EWL method. We also show in the panels on the right of Figure 2c,d the relative deviation between the 2B and 3B results for $Q(N, V, T)$. The addition of the repulsive 3-body interactions results in a decrease in the value of $Q(N, V, T)$. The effect of the 3-body

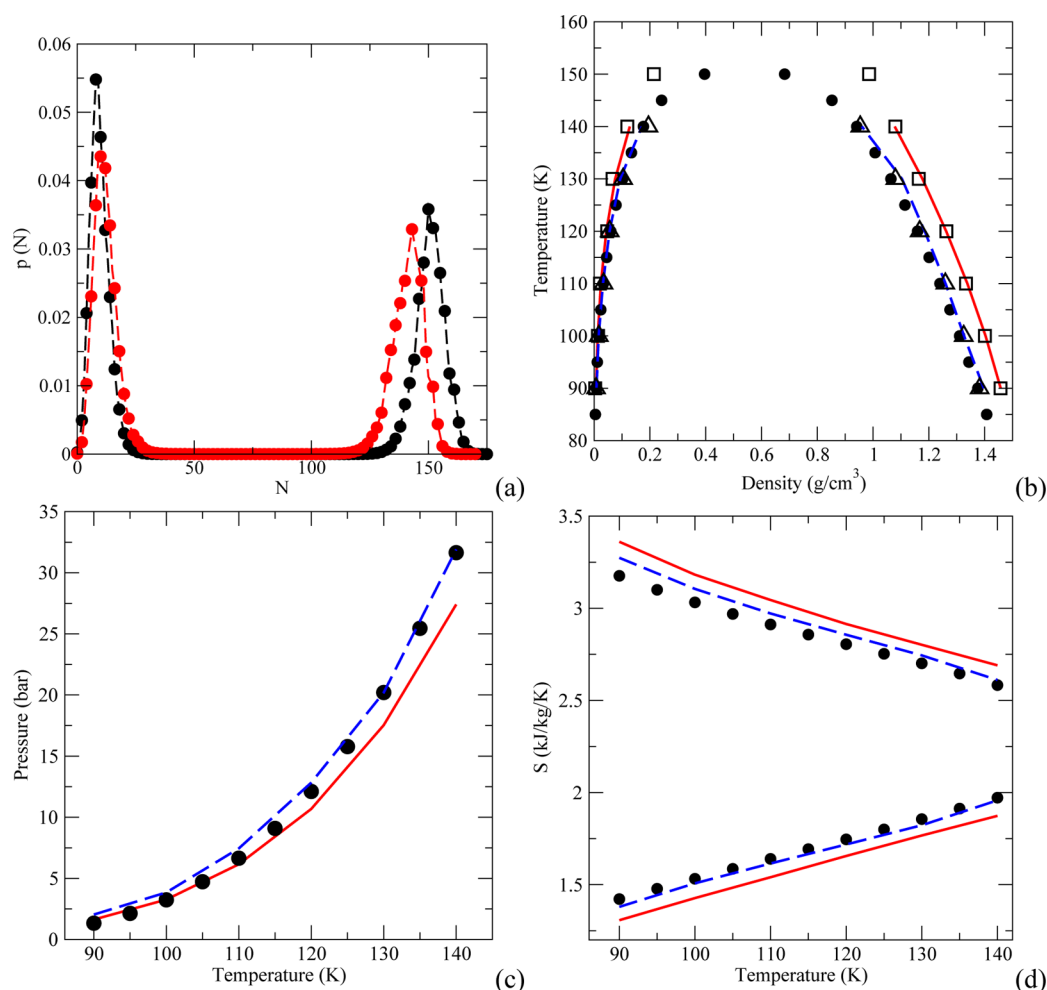


Figure 3. Liquid–vapor coexistence for argon. (a) Number probability $p(N)$ at coexistence for $T = 130$ K (black filled circles, 2B potential; red filled circles, 3B potential), (b) vapor–liquid equilibrium curve, (c) pressure at coexistence vs temperature, and (d) entropy of the coexisting phases (top, vapor; bottom, liquid) at coexistence vs temperature. Black filled circles, experimental data;⁹² red solid line, EWL results for the 2B potential; blue dashed line, EWL results for the 3B potential; open squares, 2B simulation results using the Gibbs ensemble Monte Carlo (GEMC) method;⁶⁶ and open triangles, 3B GEMC simulation results.

terms also increases steadily with the number of atoms N in the system or, equivalently, with the density. For argon, the deviation reaches about 0.1% for low N values corresponding to vapor densities and up to 2.4% for the higher values of N typical of liquid densities. Similar results are observed for krypton, with a deviation of about 0.1% for the vapor density range and a maximum deviation of 2.5% in the liquid density range. This explains why the 2B and 3B $\Theta(\mu, V, T)$ are similar for the vapor and start to depart significantly from each other only at the onset of the transition toward the liquid phase. It is also striking to note that, because of weighted sum of eq 6, the cumulation of the relative deviation for each $Q(N, V, T)$ results in much the larger deviations for $\Theta(\mu, V, T)$ shown for large μ in Figure 2a,b.

We now examine how the relative deviation between the 2B and 3B $\Theta(\mu, V, T)$ impacts the fluid properties. Starting with the vapor–liquid coexistence, we need to identify, for each temperature, the chemical potential μ_{coex} leading to equal probabilities for the two coexisting phases $\Pi_l = \Pi_v$ for the liquid and vapor phases, respectively. To achieve this, we define the number distribution $p(N)$ given by

$$p(N) = \frac{Q(N, V, T) \exp \beta \mu N}{\Theta(\mu, V, T)} \quad (11)$$

and determine numerically the value of μ_{coex} such that we have $\Pi_l = \Pi_v$, written as

$$\sum_{N < N_b} p(N) = \sum_{N > N_b} p(N) \quad (12)$$

with N_b denoting the boundary value (the value of N for which the number distribution reaches a minimum between the two peaks corresponding to the liquid and vapor phases).

A comparison between the $p(N)$ at coexistence obtained with either the 2B or 3B potential is provided in Figure 3a. We observe that the 2B potential leads to peaks that are more sharply defined, with a maximum (corresponding to the vapor phase) reached for a lower N than for the 3B potential and another maximum (corresponding to the liquid phase) reached for a higher N than for the 3B potential. This has a direct impact on the densities of the two coexisting phases. We show in Figure 3b the EWL results for the densities at coexistence for the 2B and 3B potentials. For the liquid phase, the 2B densities are significantly greater (by up to 12% at high temperature) than the 3B densities. We observe the opposite trend for the vapor phase, since the 2B densities undershoot the 3B densities by up to 25% at high temperature. Including the 3-body interactions improves the agreement of the EWL results with

experiment, with the EWL liquid densities being within 0.02 g/cm³ of the experimental liquid densities at high temperature and the EWL vapor densities being within 0.005 g/cm³ of the experiment.

The pressure at coexistence is directly impacted by the effect of the 3-body interactions on the grand-canonical partition function at coexistence. This is because the pressure P is related to $\Theta(\mu, V, T)$ through

$$P = \frac{k_B T \ln \Theta(\mu, V, T)}{V} \quad (13)$$

The EWL results for P at coexistence are shown in Figure 3c, together with the available experimental data. Including the 3-body contribution results in an increase in the chemical potential at coexistence and thus of the pressure at coexistence. The effect of the 3-body contribution on pressure is, therefore, significant, as shown by comparing the results at, e.g., $T = 130$ K, with the 2B pressure being lower by 13% than the 3B pressure. Furthermore, adding the 3-body contribution improves greatly the agreement with the experimental data, as shown in Figure 3c.

We finally examine in Figure 3d the variations of the molar entropy of the coexisting phases as a function of temperature. The molar entropy for the vapor and the liquid phases can be evaluated from $\Theta(\mu, V, T)$

$$S_{\text{liq}} = \frac{k_B \ln \Theta(\mu, V, T)}{\langle N_{\text{liq}} \rangle} + \frac{(U_{\text{liq}} - \mu)}{T}$$

$$S_{\text{vap}} = \frac{k_B \ln \Theta(\mu, V, T)}{\langle N_{\text{vap}} \rangle} + \frac{(U_{\text{vap}} - \mu)}{T} \quad (14)$$

where U_{liq} and U_{vap} denote the molar internal energy (collected during the EWL simulations) for the liquid and vapor phases, respectively, and $\langle N_{\text{liq}} \rangle$ and $\langle N_{\text{vap}} \rangle$ are the average numbers of atoms in the coexisting phases. For the liquid, the 2B entropy is lower than the 3B entropy by up to 0.08 kJ/kg/K (up to 5%). For the vapor, the 2B entropy is higher than the 3B entropy by up to 0.09 kJ/kg/K (up to 3%). This result can be rationalized in terms of the lower liquid densities obtained when including the 3-body contribution (resulting in a higher entropy for the 3B potential) and in terms of the higher vapor densities obtained with the 3-body contribution (leading to a higher entropy for the 3B potential). Once again, including the 3-body contribution improves significantly the agreement with the experimental data (see Figure 3c).

The EWL results for the partition function can also be used away from the coexistence region to determine the properties of compressed liquids. By varying the chemical potential away from its value at the vapor–liquid coexistence, we are able to calculate $\Theta(\mu, V, T)$ and thus the pressure of compressed liquids through eq 13, as well as the other thermodynamic properties. We show in Table 2 the deviation of the 2B and 3B results from the experimental data for the enthalpy and entropy. The results show that including the 3-body interactions significantly improves the agreement with the experimental data. For H , the 2B results depart more and more from the experiment as P increases, from 20% at low P up to 26% at 500 bar. On the other hand, the 3B results are much closer to the experimental data, with deviations ranging between 5 and 7% over the whole pressure range. For S , the 2B results are once again further away

Table 2. Liquid Argon at 120 K: Deviation of the EWL Results Obtained with the 2B and 3B Potentials from the Experimental Data⁹²

P (bar)	H_{exp} (kJ/kg)	2B deviation (%)	3B deviation (%)	S_{exp} (kJ/kg/K)	2B deviation (%)	3B deviation (%)
30	−78.2	20.36	5.84	1.735	−5.48	−2.02
40	−78.1	20.28	5.98	1.729	−5.15	−1.68
50	−78.0	20.17	6.05	1.729	−5.73	−2.26
60	−77.8	20.18	6.21	1.718	−5.12	−2.21
80	−77.4	20.10	6.34	1.707	−5.10	−2.17
100	−76.9	20.08	6.41	1.698	−5.18	−2.24
150	−75.4	20.04	6.25	1.676	−4.53	−2.15
200	−73.7	20.20	5.73	1.657	−4.65	−1.63
300	−69.8	22.00	5.11	1.625	−4.62	−0.92
400	−65.6	24.27	6.18	1.598	−4.88	−1.75
500	−61.0	26.00	6.89	1.573	−4.64	−1.46

from the experimental data, with deviations from 4.5 to 5.7%, whereas the 3B results exhibit much smaller deviations (between 0.9 and 2.3%).

We also present in Table 3 the relative deviations between the 2B and 3B results for the liquid. We see that, in line with

Table 3. Liquid Argon at 120 K: Relative Deviation (RD) between the EWL Results Obtained with the 2B and 3B Potentials

P (bar)	RD for A (%)	RD for G (%)	RD for U (%)
30	1.38	1.44	13.13
40	1.38	1.46	12.76
50	1.38	1.48	12.43
60	1.39	1.50	12.12
80	1.39	1.54	11.65
100	1.40	1.58	11.29
150	1.42	1.66	10.77
200	1.43	1.75	10.74
300	1.43	1.92	11.25
400	1.46	2.09	10.73
500	1.50	2.27	10.10

the results for H that showed significant differences between the 2B and 3B potentials, the relative deviation for the internal energy U ranges from 10.1 to 13.2%. However, the deviations observed for the Helmholtz and Gibbs free energies are much smaller, on the order of 1–2.5% over the pressure range considered here. The lesser sensitivity of the free energies can be attributed to a compensation of two effects. As shown in Table 2, the entropy of the liquid phase is much smaller for the 2B potential than for the 3B potential and the experiment, resulting in a smaller entropic contribution to A and G . This, coupled with the large deviations for U and H predicted by the 2B potential, results in free energies for the 2B potential that are close to those predicted by the 3B potential.

4.2. Binary Mixtures. We now turn to the analysis of the results obtained for binary mixtures. We show in Figure 4a a comparison between the EWL results for the grand-canonical partition function $\Theta(\mu_{\text{Ar}}, \mu_{\text{Kr}}, V, T)$ obtained with the 2B and 3B potentials. The partition function is now a function of two chemical potentials, μ_{Ar} and μ_{Kr} , leading to the 3D plot shown in Figure 4a. To better assess the differences in behavior between the 2B and 3B partition functions, we also plot in

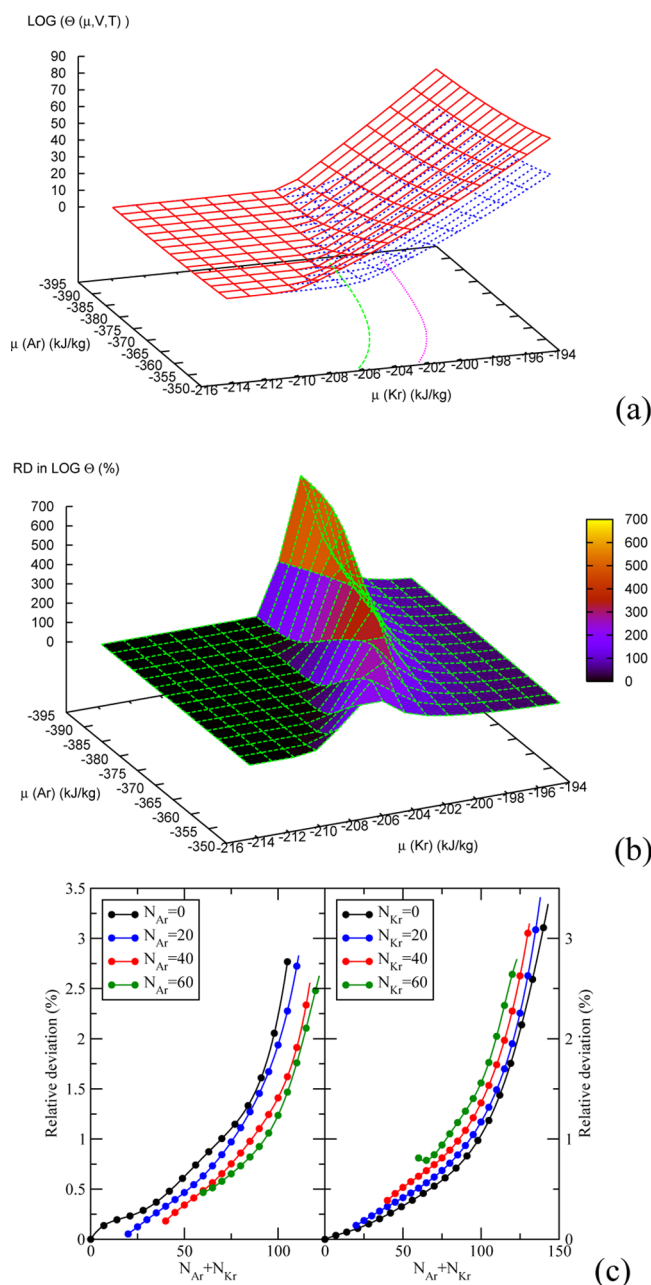


Figure 4. Argon–krypton at $T = 143.15$ K: (a) logarithm of $\Theta(\mu_{\text{Ar}}, \mu_{\text{Kr}}, V, T)$ against the chemical potential μ_{Ar} and μ_{Kr} in kJ/kg (red solid line, 2B potential; blue dashed line, 3B potential). The two contour lines in the bottom plane indicate the loci of the steep increase in $\text{LOG}(\Theta)$ for the 2B potential (in green) and for the 3B potential (in pink); (b) relative deviation in $\text{LOG}(\Theta)$ between the 2B and 3B results and (c) relative deviation in the logarithm of $Q^*(N_{\text{Ar}}, N_{\text{Kr}}, V, T) = \Lambda_{\text{Ar}}^{3N_{\text{Ar}}} \Lambda_{\text{Kr}}^{3N_{\text{Kr}}} Q(N_{\text{Ar}}, N_{\text{Kr}}, V, T)$.

Figure 4b the relative deviation between the two functions. For low μ_{Ar} and μ_{Kr} values (low-density systems), the 2B and 3B partition functions are in very good agreement. Then, as the chemical potentials increase, the partition functions start to increase sharply, with the 2B Θ increasing first, for lower chemical potentials, before the 3B Θ . This can best be seen at the bottom of Figure 4a, which shows the $(\mu_{\text{Ar}}, \mu_{\text{Kr}})$ loci corresponding to the steep increase for the 2B and 3B potentials. The increase in Θ is associated with a phase transition of the system, from the low-density vapor phase at

low $(\mu_{\text{Ar}}, \mu_{\text{Kr}})$ to the high-density liquid phase at high $(\mu_{\text{Ar}}, \mu_{\text{Kr}})$. Similarly to the case of single-component fluids, including the 3-body contributions results in a shift of the phase transition toward higher $(\mu_{\text{Ar}}, \mu_{\text{Kr}})$ values. After both systems have undergone the vapor–liquid transition, the 2B Θ and 3B Θ remain significantly different from each other, with deviations in excess of 40% for all values of μ_{Ar} at $\mu_{\text{Kr}} = -194$ kJ/kg (see the right side of Figure 4b). The partition function $\Theta(\mu_{\text{Ar}}, \mu_{\text{Kr}}, V, T)$ is calculated as a weighted sum of the $Q(N_{\text{Ar}}, N_{\text{Kr}}, V, T)$ functions (see eq 7). We show in Figure 4c the relative deviations between the 2B and 3B $Q(N_{\text{Ar}}, N_{\text{Kr}}, V, T)$ for a few different sets of $(N_{\text{Ar}}, N_{\text{Kr}})$. The deviations are on the same order as those reported for single-component fluids and can reach up to 3% in the liquid range. The large deviations observed for the partition function $\Theta(\mu_{\text{Ar}}, \mu_{\text{Kr}}, V, T)$ are, therefore, the result of the cumulation of the summed deviations in each $Q(N_{\text{Ar}}, N_{\text{Kr}}, V, T)$, as these terms become especially important for weighting factors or, equivalently, chemical potentials typical of the liquid phase.

We now measure the impact of the deviations in $\text{LOG}(\Theta)$ on the thermodynamics of mixtures. We first determine the conditions for which vapor–liquid equilibrium can be achieved. From a practical standpoint, we solve numerically eq 12 (with the sums extending, this time, over both N_{Ar} and N_{Kr}) for the sets of chemical potentials $(\mu_{\text{Ar}}, \mu_{\text{Kr}})$ leading to equal probabilities for the two phases. The EWL results so obtained are presented in Figure 5a and compared to the experimental compositions at coexistence. While the vapor–liquid equilibrium curve retains the same qualitative shape, the 3-body interactions have a strong impact on the equilibrium compositions at coexistence over the whole pressure range. For a given pressure, the 2B mole fraction in Kr (x_{Kr}) in the vapor phase is consistently less than the 3B x_{Kr} (by 21% at 10 bar and by 30% at 20 bar), whereas the 2B x_{Kr} in the liquid is less than the 3B x_{Kr} (by 7% at 10 bar and by 20% at 20 bar). When compared to the experimental data, the 3B simulation results are found to be in very good agreement with the experiment. This confirms that including the 3-body contribution results in a much improved agreement with the experimental data. Figure 5b shows the 2B and 3B densities at coexistence. In accord with the results for the vapor phase of single-component fluids at coexistence, the density of the vapor phase is consistently underestimated by the 2B potential (e.g., by 6% at 20 bar) over the whole temperature range. However, the density of the liquid phase exhibits an unexpected behavior, with a crossover from a low-pressure regime ($P < 15$ bar), in which the 3B liquid density is lower than the 2B liquid density, to a high-pressure regime ($P > 15$ bar), in which the 3B liquid density is larger than the 2B density. It is *a priori* surprising that the inclusion of the 3-body interactions results in a larger liquid density at high pressure. This can be explained by the much lower liquid mole fractions in Kr predicted by the 2B model. Neglecting the 3-body interactions essentially results in replacing heavier Kr atoms by lighter Ar atoms, leading to a lower density at high pressure.

We now examine in Table 4 the dependence of the enthalpy of vaporization ΔH_{vap} , the molar volume of the liquid V_{m}^{l} and the vapor V_{m}^{v} on pressure. As for the liquid density shown in Figure 5b, ΔH_{vap} is found to exhibit a crossover from a low-pressure regime ($P < 26.5$ bar), in which $\Delta H_{\text{vap}, 2\text{B}}$ is greater than $\Delta H_{\text{vap}, 3\text{B}}$ by up to 5.6%, to a high-pressure regime, in which $\Delta H_{\text{vap}, 2\text{B}}$ is less than $\Delta H_{\text{vap}, 3\text{B}}$ by up to 1%. The existence of the crossover between the low- and high-pressure regimes is

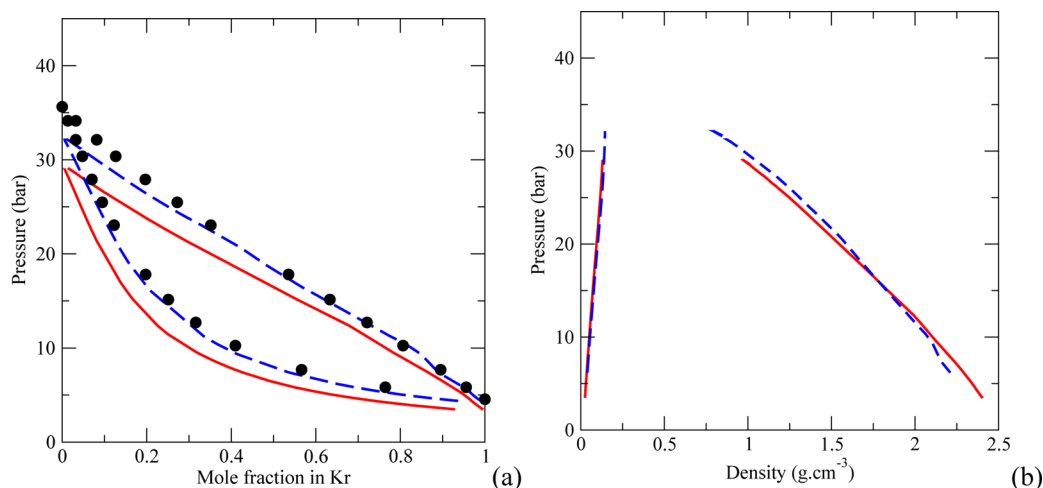


Figure 5. Vapor–liquid equilibrium of argon–krypton at $T = 143.15$ K: (a) pressure vs mole fraction in Kr and (b) pressure vs coexisting densities. Same legend as that in Figure 3.

Table 4. Vapor–Liquid Equilibrium of Argon–Krypton at $T = 143.15$ K: Relative Deviation (RD) between the EWL Results Obtained with the 2B and 3B Potentials

P (bar)	$\Delta H_{\text{vap},3\text{B}}$ (kJ/mol)	RD (%)	$V_{\text{m},3\text{B}}^{\text{L}}$ (cm ³ /mol)	RD (%)	$V_{\text{m},3\text{B}}^{\text{V}}$ (cm ³ /mol)	RD (%)
6.2	8.51	5.6	36.6	−4.8	1734.1	2.3
12.4	7.47	4.7	36.7	−4.6	810.8	1.5
14.5	7.06	4.1	36.8	−4.6	670.9	2.3
18.0	6.41	3.6	37.1	−4.6	520.5	3.5
21.4	5.82	1.7	37.7	−4.4	421.4	3.2
25.0	5.10	1.0	38.9	−3.6	348.6	3.5
27.9	4.52	−0.9	41.1	−2.3	310.9	3.2
28.8	4.29	−0.3	42.3	−2.4	301.5	3.5

again unexpected, as one would expect the repulsive 3-body interactions to result in a systematic lower ΔH_{vap} for the 3B potential than for the 2B potential. Given that ΔH_{vap} for pure Kr is roughly twice that of pure Ar, the crossover can be attributed to the fact that the 2B potential underestimates the mole fraction in Kr and essentially replaces more and more Kr atoms by Ar atoms as the pressure increases.

Table 4 also shows that the 2B molar volume for the liquid is consistently smaller than its 3B counterpart. This is consistent with what one would expect, as the 3-body interactions are repulsive and naturally lead to fewer atoms per unit volume. Therefore, the crossover observed in Figure 5b between the 2B and 3B mass densities is not correlated with a crossover in the molar density. This confirms that the decrease in the 2B density with pressure is due to the inability of the 2B potential to provide an accurate estimate for the Kr mole fraction. The molar volume for the vapor V_{m}^{V} exhibits the expected behavior, i.e., consistently larger values for the 2B potential than for the 3B potential, which includes the repulsive 3-body interactions.

We also compare the 2B and 3B chemical potentials obtained for Ar and Kr in Table 5. For Kr, including the 3-body term results in a greater μ_{Kr} over the whole range of conditions (by 2% at low pressure and by up to 11% at high pressure), whereas for Ar, the 3-body contribution leads to smaller G (by 2% at low pressure and by 0.2% at high pressure). In both cases, the impact of the 3-body interactions on the chemical potential is most significant when the mole fraction is very low, i.e., when the element considered (Ar or Kr) can be regarded as the

Table 5. Chemical Potentials at Coexistence for the Binary Mixture Argon–Krypton at $T = 143.15$ K: Relative Deviation (RD) between the EWL Results Obtained with the 2B and 3B Potentials

P (bar)	$\mu_{\text{Ar},3\text{B}}$ (kJ/kg)	RD (%)	$\mu_{\text{Kr},3\text{B}}$ (kJ/kg)	RD (%)
6.2	−403.96	2.2	−200.16	−1.7
12.4	−363.92	0.8	−203.07	−2.0
14.5	−357.37	0.6	−204.35	−2.1
18.0	−349.48	0.4	−206.83	−2.3
21.4	−343.67	0.4	−209.81	−2.9
25.0	−338.61	0.3	−214.43	−4.1
27.9	−335.18	0.3	−220.46	−7.4
28.8	−334.14	0.2	−223.37	−10.4

solute, as shown here in binary mixtures at high pressure in the case of Kr and at low pressure in the case of Ar. This result emphasizes the significance of the role of the 3-body contribution to the solvation free energy.

4.3. Nanoconfined Single-Component Fluids. The results obtained for the grand-canonical partition function of nanoconfined argon are shown at $T = 100$ K in Figure 6a for the 2B and 3B potentials, together with the relative deviation in $\log(\Theta)$ between the 2B and 3B results. As for bulk systems, the 2B and 3B results are in excellent agreement for low μ_{Ar} values, i.e., when the density of the nanoconfined fluid is very low. Then, the 2B grand-canonical partition increases sharply at first (for $\mu_{\text{Ar}} > -291.8$ kJ/kg), followed by the steep increase of the 3B grand-canonical partition function (for $\mu_{\text{Ar}} > -288.7$ kJ/kg). The delayed response in $\log(\Theta)$ between the 2B and 3B potentials can best be seen on the right panel of Figure 6a, with the maximum deviation of about 200% observed for a chemical potential $\mu_{\text{Ar}} = -289.12$ kJ/kg. The steep increase in $\log(\Theta)$ is associated with a transition from a low-density adsorbed phase, with few Ar atoms adsorbed in the nanopore, to a high-density adsorbed phase, with a large number of Ar atoms adsorbed. As μ_{Ar} further increases, both the 2B and 3B potentials lead to a high-density adsorbed phases with a relative deviation for $\log(\Theta)$ that remains significant throughout the range of μ_{Ar} values (e.g., 12.2% for $\mu_{\text{Ar}} = -250$ kJ/kg). We also show in Figure 6b the values of $Q(N_{\text{Ar}}, V, T)$ predicted by the 2B and 3B potentials. We find that the 3B potential results in a decrease in $\log Q(N_{\text{Ar}}, V, T)$ of up to a few tenths of a percent for low-

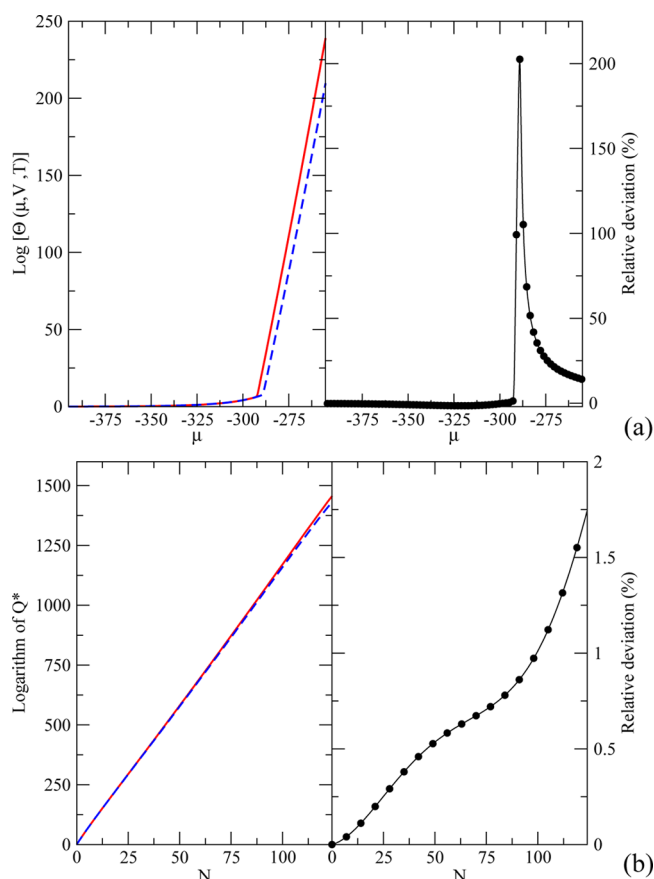


Figure 6. Argon adsorbed in a slit nanopore at $T = 100$ K. (a) (left) Logarithm of $\Theta(\mu_{\text{Ar}}, V, T)$ against the chemical potential μ_{Ar} in kJ/kg (red solid line, 2B potential; blue dashed line, 3B potential) and (right) relative deviation in $\log(\Theta)$ between the 2B and 3B results. (b) (left) Logarithm of $Q^*(N_{\text{Ar}}, V, T) = \Lambda_{\text{Ar}}^{3N_{\text{Ar}}} Q(N_{\text{Ar}}, V, T)$ against the chemical potential μ_{Ar} (same legend as in (a)) and (right) relative deviation in the logarithm of $Q^*(N_{\text{Ar}}, V, T)$.

density adsorbed phases (low N_{Ar} values) and of up to 1.8% for high-density adsorbed phases. This is consistent with the results

obtained for the 2B and 3B $\Theta(\mu, V, T)$, which are similar for the vapor and start to depart significantly from each other only at the onset of the transition toward high-density nanoconfined Ar. The large deviations for $\Theta(\mu, V, T)$ for large μ (high-density nanoconfined Ar) can be attributed to the cumulative effect, when calculating the weighted sum of eq 6, of the relative deviations for each $Q(N, V, T)$ at large N_{Ar} values.

We now turn to the effect of nanoconfinement on the number distribution for the 2B and 3B potentials. We show in Figure 7a $p(N)$ against the number of Ar atoms adsorbed in the nanopore. For both potentials, the number distribution exhibits two peaks, corresponding to the coexistence of a low-density nanoconfined phase (akin to the vapor phase of the bulk) and of a high-density phase (akin to the liquid). Compared to the 3B number distribution, and in line with the results for the vapor–liquid coexistence for the bulk, the extrema for the 2B $p(N)$ are reached at a lower value of N_{Ar} for the low-density phase and at a larger value of N_{Ar} for the high-density phase.

This has a direct impact on the phase diagram of nanoconfined Ar. To allow for a comparison between the phase diagram for the bulk and for the nanoconfined fluid, we first need to determine the density of the two nanoconfined phases from the number distribution $p(N)$. This requires defining the volume V_{void} of the nanopore accessible to the fluid. We use the same definition as that introduced by Myers and Monson^{93–95} to calculate the accessible volume for the pore and find a value of $V_{\text{void}} = 0.973V$ (V being the total volume of the nanopore considered here). The phase diagram so obtained for nanoconfined Ar is plotted in Figure 7b and compared to the experimental data for the bulk as well as to the EWL results for the bulk. At a given temperature, nanoconfinement has a strong impact on phase coexistence. It has the effect of increasing the density of the vapor at coexistence (e.g., by 82% at $T = 100$ K for the 2B potential) and of decreasing the density of the liquid at coexistence (by 28% at $T = 100$ K for the 2B potential). As for the bulk, the phase envelope for the 3B potential remains inside the 2B phase envelope, as the 2B potential overshoots (by 21% at $T = 100$ K) the 3B results for the high-density adsorbed phase and undershoots (by 6% at $T = 100$ K) the 3B results for the low-density adsorbed phase.

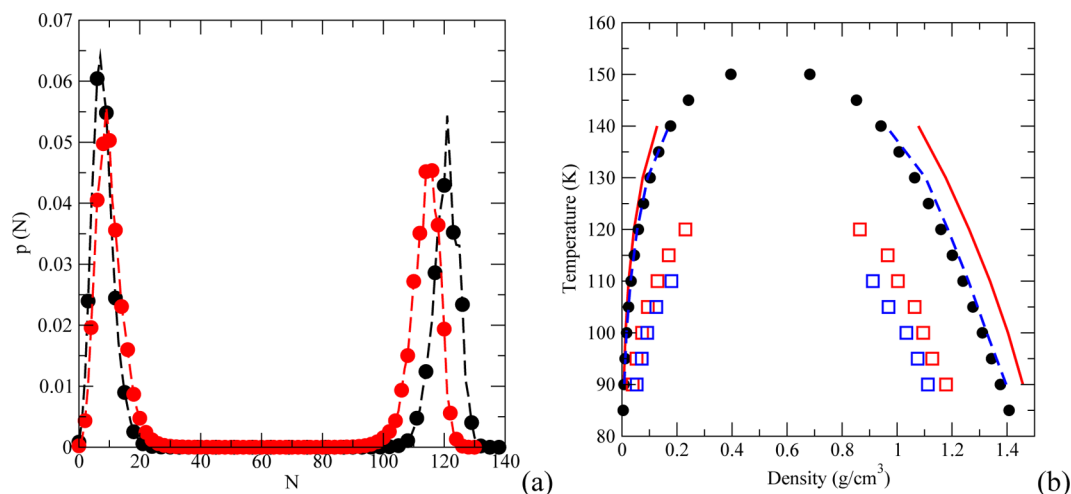


Figure 7. Vapor–liquid equilibrium for nanoconfined argon: (a) number probability $p(N)$ at coexistence for $T = 100$ K (black filled circles, 2B potential; red filled circles, 3B potential) and (b) vapor–liquid equilibrium curve. Black filled circles are the experimental data for the bulk,⁹² lines are the EWL results for the bulk (red solid line, 2B results; blue dashed line, 3B results), and open symbols are the EWL results for nanoconfined argon (open red squares, 2B results; open blue squares, 3B results).

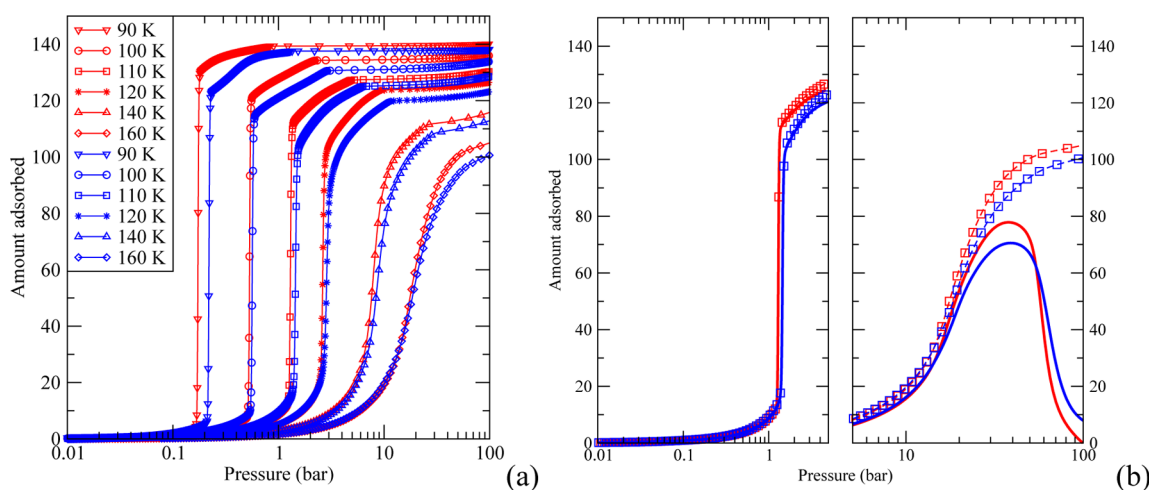


Figure 8. Adsorption isotherm for argon in a slit nanopore. (a) 2B and 3B absolute adsorption isotherms showing $\langle N_{\text{adsorbed}} \rangle$ vs pressure and (b) absolute ($\langle N_{\text{adsorbed}} \rangle$) and excess ($\langle N_{\text{adsorbed}}^e \rangle$) adsorption isotherms. (left) Subcritical isotherms at $T = 110$ K and (right) supercritical isotherms at $T = 160$ K. Open symbols are for the absolute isotherms, and solid lines are for the excess isotherms (red, 2B results; blue, 3B results).

We move on to the analysis of the thermodynamic properties of adsorption and start by determining the adsorption isotherms. For this purpose, we vary the chemical potential μ and determine the number of Ar atoms adsorbed in the nanopore from the number distribution $p(N)$ as $\langle N_{\text{adsorbed}} \rangle = \sum N p(N)$. This defines the absolute adsorption isotherms shown in Figure 8a for the 2B and 3B potentials for temperatures ranging from 90 to 160 K. The general features of the adsorption isotherms can be described as follows: As T increases, the amount adsorbed at a given pressure decreases (e.g., by 25% when T increases from 90 to 160 K at $P = 100$ bar for the 2B potential). The pressure at which the amount adsorbed increases rapidly is also found to increase with temperature (e.g., from 0.18 bar at $T = 90$ K to 2.71 bar at $T = 120$ K for the 2B potential). Furthermore, the shape of the adsorption isotherm evolves as we move from the subcritical regime, in which the isotherm exhibits a sharp step, to the supercritical regime, in which the number of atoms adsorbed increases more smoothly (see, e.g., the isotherms for $T = 140$ and 160 K). Compared to the 2B potential, the 3B potential results in absolute adsorption isotherms exhibiting a shift in the adsorption step toward the higher pressures (e.g., by 6.5% at $T = 90$ K) and a lower maximum amount adsorbed at a given pressure (e.g., by 4.3% at $T = 120$ K and $P = 100$ bar). This can be attributed to the fact that the 3-body interactions are repulsive, which, in turn, leads to an increase in pressure and a decrease in the density of the nanoconfined fluid.

We also determine the excess adsorption isotherm from the excess number of Ar atoms adsorbed $\langle N_{\text{adsorbed}}^e \rangle$. The excess adsorption isotherms are of particular significance, since experiments provide access only to excess adsorption properties.⁹³ The excess number is defined as the number of Ar atoms adsorbed in the accessible volume V_{void} of the nanopore relative to the gas phase under the same thermodynamic conditions. This gives $\langle N_{\text{adsorbed}}^e \rangle = \langle N_{\text{adsorbed}} \rangle - \rho_g V_{\text{void}}$ in which ρ_g is the gas density calculated from EWL simulations on the bulk vapor of Ar for the same chemical potential μ and temperature T . A comparison between the absolute and excess adsorption isotherms is shown in Figure 8b for the 2B and 3B potentials. At $T = 110$ K, the adsorption and excess adsorption isotherms overlap almost perfectly, which is typical of subcritical adsorption. This is due to the fact that, at $T = 110$ K, the

density of the gas phase remains very small over the pressure range, both for the 2B and 3B potentials, leading to virtually the same numbers for $\langle N_{\text{adsorbed}}^e \rangle$ and $\langle N_{\text{adsorbed}} \rangle$. However, at $T = 160$ K, the excess adsorption isotherms are markedly different from the absolute adsorption isotherm, as they exhibit a maximum (reached at $P = 38$ bar for the 2B potential and at $P = 39$ bar for the 3B potential) characteristic of the supercritical regime.⁹³ Unlike the absolute adsorption isotherm, which increases steadily with P , the excess adsorption isotherms start to increase with P , as the density of nanoconfined Ar increases faster than the bulk density^{64,93,94} at low P . Then, as the nanopore starts to become saturated with the adsorbed Ar, the density of nanoconfined Ar increases much more slowly than the bulk density^{64,93,94} at higher P , leading to the decrease in the excess adsorption isotherms. The excess amount adsorbed predicted by the 2B potential is greater than that given by the 3B potential for $P < 53$ bar. We observe the reverse, however, at $P > 53$ bar, with the excess amount adsorbed predicted by the 3B potential exceeding the 2B prediction. This unexpected result stems for the reduced rate at which the 3B gas (bulk) density increases with P due to the inclusion of the repulsive 3-body interactions. This results in a slower decrease in $\langle N_{\text{adsorbed}}^e \rangle$ for the 3B potential as compared to that for the 2B potential.

We complete our analysis of the thermodynamic of nanoconfined Ar by determining the excess Gibbs free energy ΔG^e , entropy ΔS^e , and enthalpy ΔH^e of nanoconfined Ar. For each property B ($B = S, G, H$), the excess properties ΔB^e is obtained using the following relations

$$\Delta B^e = B - V_{\text{void}} \overline{B}^g \rho_g \quad (15)$$

in which the molar property for the gas phase \overline{B}^g and the absolute property of the adsorbed fluid B are obtained from the EWL partition functions for each system under the same thermodynamic conditions.

We compare in Table 6 the results obtained for $-\Delta H^e$, $T\Delta S^e$, and $-\Delta G^e$ with the 2B and 3B potentials in the subcritical regime ($T = 110$ K) and in Table 7 for the supercritical regime ($T = 160$ K). At high pressure, after the isotherm step, $-\Delta H^e$ is found to be greater for the 2B potential than for the 3B potential (e.g., by 6% at 4 bar for $T = 110$ K and by 6.9% at 50 bar for $T = 160$ K). This can be attributed to the lower density of nanoconfined Ar for the 3B potential, which results from the

Table 6. Excess Properties for Nanoconfined Ar in the Subcritical Regime ($T = 110$ K): EWL Results for the 3B Potential and Relative Deviation (RD) between the EWL Results Obtained with the 2B and 3B Potentials

P (bar)	$-\Delta H_{3B}^e$ (kJ/mol)	RD (%)	$T\Delta S_{3B}^e$ (kJ/mol)	RD (%)	$-\Delta G_{3B}^e$ (kJ/mol)	RD (%)
0.2	3.11	0.6	10.03	−0.3	13.14	0.0
0.5	2.59	0.0	9.96	−0.2	12.55	−0.2
0.8	2.52	−1.2	9.82	0.1	12.34	−0.1
1	2.55	−1.6	9.69	0.4	12.24	0.0
1.5	4.74	13.3	7.38	−6.9	12.12	0.9
2	5.12	8.2	6.96	−4.3	12.08	1.0
3	5.36	6.7	6.65	−3.5	12.01	1.0
4	5.47	6.0	6.47	−3.1	11.94	1.2

Table 7. Excess Properties for Nanoconfined Ar in the Supercritical Regime ($T = 160$ K): EWL Results for the 3B Potential and Relative Deviation (RD) between the EWL Results Obtained with the 2B and 3B Potentials

P (bar)	$-\Delta H_{3B}^e$ (kJ/mol)	RD (%)	$T\Delta S_{3B}^e$ (kJ/mol)	RD (%)	$-\Delta G_{3B}^e$ (kJ/mol)	RD (%)
2	2.01	3.0	12.42	−2.1	14.43	−1.4
6	1.77	1.1	12.67	−0.2	14.45	−0.1
10	1.90	−1.1	12.40	0.2	14.30	0.1
20	2.77	5.1	11.44	0.1	14.20	1.1
30	3.44	7.8	10.18	−1.0	13.61	1.3
40	3.73	8.0	9.01	−1.2	12.74	1.5
50	3.89	6.9	7.60	−3.9	11.48	−0.2

inclusion of the repulsive 3-body interactions. Similarly, we find the excess entropy ΔS^e to decrease with P , as a result of the increase in the density of the nanoconfined fluid. For ΔS^e , the 3-body contribution leads to a higher excess entropy (by 3.1% at 4 bar for $T = 110$ K and by 3.9% at 50 bar for $T = 160$ K). This is also due to the decrease in density, obtained by taking into account the 3-body interactions, which, in turn, leads to a decrease in entropy. While the 3-body interactions have a strong impact on many of the adsorption properties (amounts adsorbed, enthalpies, and entropies), the relative deviation in the excess adsorption Gibbs free energy between the 2B and 3B potentials is surprisingly small (less than 1.5% over the range of pressures, both for the subcritical and supercritical regimes). This is due to the fact that the relative deviations between the 2B and 3B results are of opposite signs for the entropic and enthalpic contributions to the $-\Delta G^e$ and thus partially compensate each other.

4.4. Nanoconfined Binary Mixtures. We now discuss the results obtained for the nanoconfined Ar–Kr mixture, starting with the grand-canonical partition function of the adsorbed mixture. The logarithm of $\Theta(\mu_{Ar}, \mu_{Kr}, V, T)$ is shown in Figure 9a for the 2B and 3B potentials. The agreement between the two models is very good at the lower end of the range for the chemical potentials considered here, which corresponds to a low-density nanoconfined mixture. Then, as the chemical potentials increase, the 2B grand-canonical partition function increases first, followed by the 3B grand-canonical partition function. The delayed increase in $\log \Theta$, when including the 3-body contribution, results in a domain of chemical potentials (μ_{Ar}, μ_{Kr}) for which the 2B and 3B grand-canonical partition functions depart notably from each other, as shown in Figure 9b, with relative deviations in $\log \Theta$ reaching more than 20% for the range of chemical potentials plotted there. Afterward,

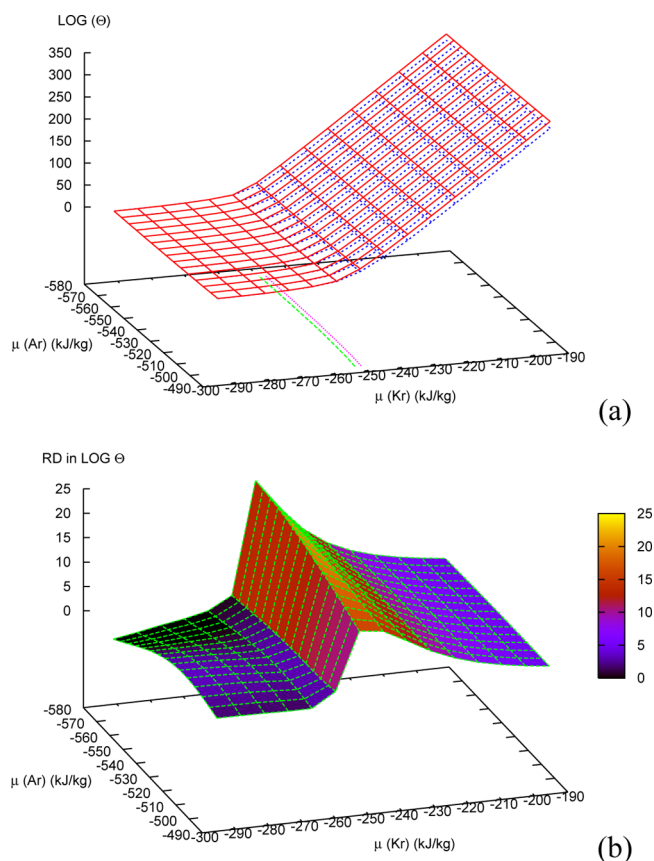


Figure 9. Argon–krypton in a slit nanopore at $T = 180$ K: (a) logarithm of $\Theta(\mu_{Ar}, \mu_{Kr}, V, T)$ against the chemical potential μ_{Ar} and μ_{Kr} in kJ/kg (red solid line, 2B potential; blue dashed line, 3B potential). The two contour lines in the bottom plane indicate the loci of the steep increase in $\log(\Theta)$ for the 2B potential (in green) and for the 3B potential (in pink). (b) Relative deviation in $\log(\Theta)$ between the 2B and 3B results.

for higher chemical potentials, the difference between the 2B and 3B partition functions remains significant, in excess of 5% for the higher end of the range shown in Figure 9b. As with the systems discussed in the previous sections, this increase in Θ is associated with the transition from a low-density nanoconfined phase to a high-density nanoconfined phase. As a result of the delayed increase in Θ for the 3B potential, the transition toward the high-density nanoconfined phase is shifted toward higher (μ_{Ar}, μ_{Kr}) values.

The number distributions $p(N_{Ar}, N_{Kr})$, obtained with the 2B and 3B potentials, are shown in Figure 10a,b for a nanoconfined Ar–Kr mixture for a set of chemical potentials corresponding to a gas pressure of $P = 12$ bar. The contour plots indicate a shift, when switching from the 2B potential to the 3B potential, in the region of (N_{Ar}, N_{Kr}) where the maximum probability is reached. Under these conditions, a maximum is observed for ($N_{Ar} = 17, N_{Kr} = 56$) for the 2B potential, whereas the maximum takes place at much lower N_{Ar} and N_{Kr} ($N_{Ar} = 12, N_{Kr} = 38$) in the case of the 3B potential. This example of the shift in numbers of atoms adsorbed, observed here for a specific set of conditions, shows that the 3-body term will lead to notable differences in the adsorption isotherms for the binary system Ar–Kr. One way to assess these differences is to vary the composition of the binary Ar–Kr gas mixture (with y_{Ar} corresponding to the mole fraction in Ar in the gas mixture) in equilibrium with the nanoconfined

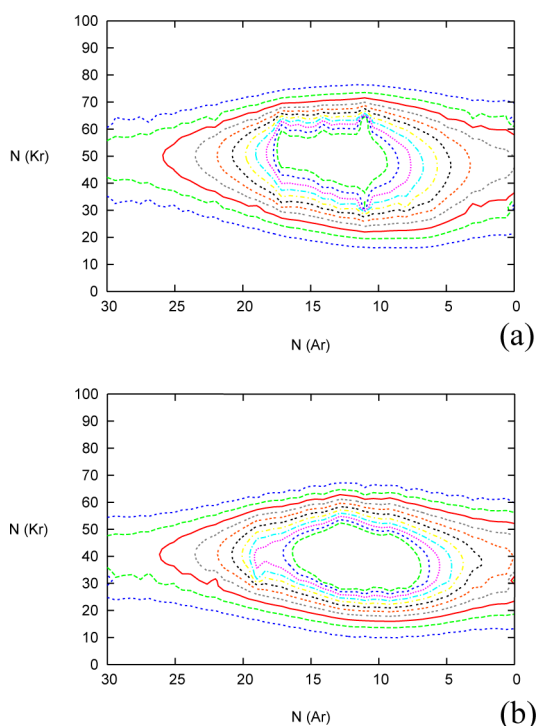


Figure 10. Argon–krypton in a slit nanopore at $P = 12$ bar and $T = 180$ K: number distribution for the (a) 2B and (b) 3B potentials.

fluid and to analyze the adsorption properties of the nanoconfined fluid for a given value of y_{Ar} .

Figure 11 shows the adsorption isotherms obtained for two different compositions of the gas phase in equilibrium with the nanoconfined mixture. For both gas compositions, the nanoconfined mixture is composed predominantly of Kr, as a result of the greater strength of the interaction between the wall and the Kr atoms ($\epsilon_{\text{w-Kr}}$ is greater than $\epsilon_{\text{w-Ar}}$ by more than 15%). Including the 3-body interactions results in a decrease of the overall amount adsorbed (by 7.6% at 20 bar for $y_{\text{Ar}} = 0.5$ and by 6.3% at 20 bar for $y_{\text{Ar}} = 0.3$). This is mostly due to the decrease in the amount of Kr adsorbed in the nanopore when switching from the 2B potential to the 3B potential. The amount of Kr adsorbed is 8.5% less for $y_{\text{Ar}} = 0.5$ and 7.5% less for $y_{\text{Ar}} = 0.5$ with the 3B potential (both data are for $P = 20$

bar), whereas the number of Ar atoms adsorbed is much less sensitive to the 3-body interactions, with differences between the 2B and 3B results on the order of about ± 1 atom adsorbed for Ar.

The differences observed in the adsorption isotherms of Ar and Kr imply that the 3-body contribution has a significant impact on the pore selectivity toward one of the adsorbates. The Kr pore selectivity is defined as

$$S_{\text{Kr}} = (x_{\text{Kr}}/x_{\text{Ar}})/(y_{\text{Kr}}/y_{\text{Ar}}) \quad (16)$$

in which x_{Kr} and x_{Ar} denote the mole fractions in the nanoconfined fluid, whereas y_{Kr} and y_{Ar} are the mole fractions in the gas phase in equilibrium with the nanoconfined fluid.

The results obtained for the selectivity S_{Kr} are given in Table 8 for different compositions of the gas mixture in equilibrium

Table 8. Selectivity for a Nanoconfined Ar–Kr Mixture at $T = 180$ K: EWL Results for the 3B Potential and Relative Deviation (RD) between the EWL Results Obtained with the 2B and 3B Potentials

P (bar)	S_{Kr} ($y_{\text{Ar}} = 0.5$)	RD (%)	S_{Kr} ($y_{\text{Ar}} = 0.6$)	RD (%)	S_{Kr} ($y_{\text{Ar}} = 0.7$)	RD (%)
2	2.31	−10.0	2.28	−8.3	2.26	−6.2
4	2.32	−3.9	2.26	−1.3	2.22	1.4
8	2.49	4.8	2.37	5.5	2.30	4.8
12	3.31	12.7	2.80	4.6	2.55	0.0
16	3.88	9.5	3.51	12.5	3.01	3.3
20	4.01	4.5	3.96	3.8	3.59	8.9

with the nanoconfined fluid. The selectivity is found to be greater than 1, which is consistent with the stronger interaction of Kr (as compared to Ar) with the confining walls. For all compositions of the gas mixture, S_{Kr} is found to exhibit a nonmonotonic dependence upon pressure. Increasing the mole fraction of argon in the gas mixture leads to a slight decrease in the selectivity S_{Kr} at a given pressure, with S_{Kr} at 20 bar decreasing by 10.5% when increasing y_{Ar} from 0.5 to 0.7. Overall, the 3-body contribution overall results in a decrease in S_{Kr} , and this effect becomes more pronounced as y_{Ar} increases. For instance, for $y_{\text{Ar}} = 0.7$ and $P = 20$ bar, we find a maximum deviation of 8.9% between the 2B S_{Kr} and the 3B selectivity, as a result of the marked decrease in the number of Kr atoms

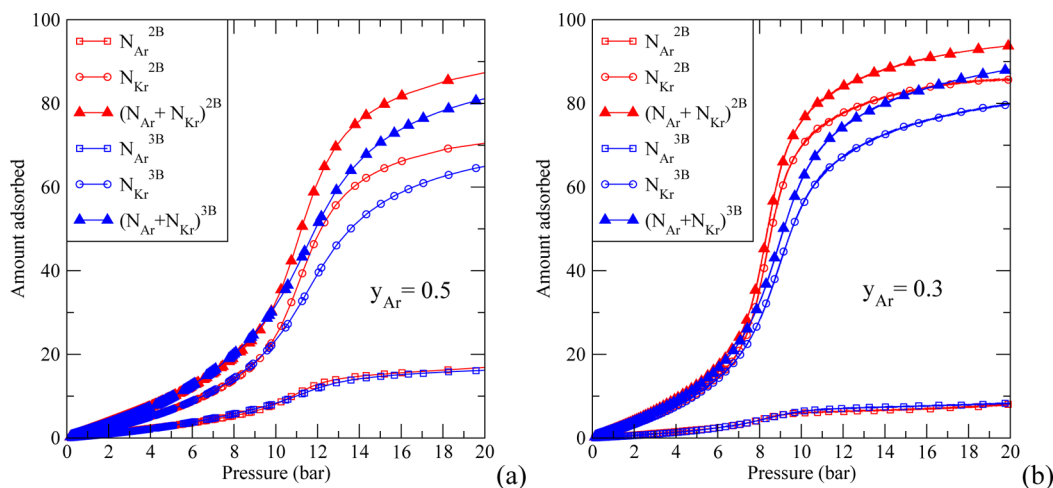


Figure 11. Argon–krypton in a slit nanopore at $T = 180$ K: adsorption isotherms for (a) $y_{\text{Ar}} = 0.5$ and (b) $y_{\text{Ar}} = 0.3$.

adsorbed when the 3-body contribution is included. This shows that the 3-body interactions has a nontrivial impact on the selectivity in nanopores.

5. CONCLUSIONS

In this work, we evaluate the contribution of the 3-body interactions to the grand-canonical partition function for single-component systems, binary mixtures, and nanoconfined phases. While the 2B and 3B partition functions are in very good agreement for low μ values (corresponding to low-density phases), these two functions start to depart from each other as μ increases. Including the 3-body interactions induces a shift toward higher chemical potentials of the transition from the low-density phase to the high-density phase, either as a vapor to a liquid for bulk fluids and mixtures or as a low-density adsorbed phase to a high-density phase for nanoconfined systems. The 3-body contribution to the partition function remains significant as μ further increases, remaining greater than 20% for single-component systems over the range of chemical potentials studied here. The analysis of the two terms involved in the definition of the grand-canonical partition function, i.e., the μ -dependent weighting factor $\exp[\beta\mu N]$ and the $Q(N,V,T)$ functions, shows the pivotal role played by the weighting factor in the sum. The EWL results show that, for all systems, the 3-body contribution to $\log Q(N,V,T)$ reaches up to 3% for large N values. Therefore, the large 3-body contribution to Θ results from the accumulation of the weighted 3-body contributions to $Q(N,V,T)$, which become significant only for large μ (or large $\exp[\beta\mu N]$). The formalism of statistical mechanics then allows for a rapid evaluation of all thermodynamic properties, once the partition functions have been evaluated. This allows us to connect the deviations for the partition functions, resulting from the inclusion of the 3-body term, to deviations in the predicted thermodynamic properties. The 3-body contribution is found to depend strongly on the type of property as well as on the type of system. For instance, at coexistence and for single-component systems, including the 3-body interaction decreases the liquid density by up to 12%, increases the vapor density by up to 25%, and increases pressure by up to 13%. Similarly, for binary mixtures, the mole fraction at a given pressure is found to be especially sensitive to the 3-body interactions, with deviations up to 30%. For nanoconfined systems, the 3-body contribution to the adsorption isotherm reaches up to 10%, and the selectivity is also significantly impacted by the 3-body interactions with deviations of up to 9% for a given mole fraction y_{Ar} . On the other hand, the 3-body contributions have a moderate impact on other properties, like the Gibbs and Helmholtz free energies, as a result of a compensation between the 3-body contributions to the entropic and enthalpic terms. While the full extent of the many-body effects will depend on the nature of the system studied, the results on noble gases presented here suggest that many-body interactions will have a significant impact on phase transitions in molecular systems as well as on the thermodynamic properties of inhomogeneous systems, such as, e.g., nanoconfined molecular systems.

AUTHOR INFORMATION

Corresponding Author

*E-mail: jerome.delhommelle@und.edu. Phone: 701-777-2495.

Funding

Partial funding for this research was provided by the NSF through CAREER award DMR-1052808.

Notes

The authors declare no competing financial interest.

REFERENCES

- (1) Jorgensen, W. L.; Maxwell, D. S.; Tirado-Rives, J. *J. Am. Chem. Soc.* **1996**, *118*, 11225–11236.
- (2) Cornell, W. D.; Cieplak, P.; Bayly, C.; Gould, I. R.; Merz, K. M.; Ferguson, D. M.; Spellmeyer, D. C.; Fox, T.; Caldwell, J. W.; Kollman, P. A. *J. Am. Chem. Soc.* **1995**, *117*, 5179.
- (3) Baker, C. M.; Lopes, P. E.; Zhu, X.; Roux, B.; MacKerell, A. D., Jr. *J. Chem. Theory Comput.* **2010**, *6*, 1181.
- (4) Sun, H. *J. Phys. Chem. B* **1998**, *102*, 7338–7364.
- (5) Oostenbrink, C.; Villa, A.; Mark, A. E.; Van Gunsteren, W. F. *J. Comput. Chem.* **2004**, *25*, 1656–1676.
- (6) Hobza, P.; Kabeláč, M.; Šponer, J.; Mejzlík, P.; Vondrášek, J. *J. Comput. Chem.* **1997**, *18*, 1136–1150.
- (7) Rappé, A. K.; Casewit, C. J.; Colwell, K.; Goddard, W., III; Skiff, W. *J. Am. Chem. Soc.* **1992**, *114*, 10024–10035.
- (8) Martin, M. G.; Siepmann, J. I. *J. Phys. Chem. B* **1998**, *102*, 2569–2577.
- (9) Wick, C. D.; Stubbs, J. M.; Rai, N.; Siepmann, J. I. *J. Phys. Chem. B* **2005**, *109*, 18974–18982.
- (10) Lubna, N.; Kamath, G.; Potoff, J. J.; Rai, N.; Siepmann, J. I. *J. Phys. Chem. B* **2005**, *109*, 24100–24107.
- (11) Errington, J. R.; Panagiotopoulos, A. Z. *J. Phys. Chem. B* **1999**, *103*, 6314–6322.
- (12) Ungerer, P.; Beauvais, C.; Delhommelle, J.; Boutin, A.; Rousseau, B.; Fuchs, A. H. *J. Chem. Phys.* **2000**, *112*, 5499.
- (13) Joung, I. S.; Cheatham, T. E., III *J. Phys. Chem. B* **2008**, *112*, 9020–9041.
- (14) Axilrod, B. M.; Teller, E. *J. Chem. Phys.* **1943**, *11*, 299–300.
- (15) Axilrod, B. M. *J. Chem. Phys.* **1951**, *19*, 724–729.
- (16) Tao, J.; Perdew, J. P.; Ruzsinszky, A. *Proc. Natl. Acad. Sci. U. S. A.* **2012**, *109*, 18–21.
- (17) DiStasio, R. A., Jr; Gobre, V.; Tkatchenko, A. *J. Phys.: Condens. Matter* **2014**, *26*, 213202.
- (18) Nasrabad, A. E.; Laghaei, R.; Deiters, U. K. *J. Chem. Phys.* **2004**, *121*, 6423–6434.
- (19) Moosavi, M.; Goharshadi, E. K. *Fluid Phase Equilib.* **2008**, *274*, 51–58.
- (20) Song, B.; Wang, X.; Wu, J.; Liu, Z. *Mol. Phys.* **2011**, *109*, 1607–1615.
- (21) Malijevský, A.; Karlický, F.; Kalus, R.; Malijevský, A. *J. Phys. Chem. C* **2007**, *111*, 15565–15568.
- (22) Nasrabad, A. E.; Laghaei, R. *J. Chem. Phys.* **2006**, *125*, 084510.
- (23) Jäger, B.; Hellmann, R.; Bich, E.; Vogel, E. *J. Chem. Phys.* **2011**, *135*, 084308.
- (24) del Río, F.; Díaz-Herrera, E.; Guzmán, O.; Moreno-Razo, J. A.; Ramos, J. E. *J. Chem. Phys.* **2013**, *139*, 184503.
- (25) Guzman, O.; del Río, F.; Eloy Ramos, J. *Mol. Phys.* **2011**, *109*, 955–967.
- (26) Cencek, W.; Garberoglio, G.; Harvey, A. H.; McLinden, M. O.; Szalewicz, K. *J. Phys. Chem. A* **2013**, *117*, 7542–7552.
- (27) Sadus, R. J. *Fluid Phase Equilib.* **1998**, *144*, 351–359.
- (28) Wiebke, J.; Pahl, E.; Schwerdtfeger, P. *J. Chem. Phys.* **2012**, *137*, 064702.
- (29) Tang, L.-Y.; Yan, Z.-C.; Shi, T.-Y.; Babb, J. F.; Mitroy, J. *J. Chem. Phys.* **2012**, *136*, 104104.
- (30) Wiebke, J.; Wormit, M.; Hellmann, R.; Pahl, E.; Schwerdtfeger, P. *J. Phys. Chem. B* **2014**, *118*, 3392–3400.
- (31) Eckl, B.; Vrabec, J.; Hasse, H. *J. Phys. Chem. B* **2008**, *112*, 12710–12721.
- (32) Tkatchenko, A.; Scheffler, M. *Phys. Rev. Lett.* **2009**, *102*, 073005.
- (33) Tkatchenko, A.; DiStasio, R. A., Jr; Car, R.; Scheffler, M. *Phys. Rev. Lett.* **2012**, *108*, 236402.

- (34) Pai, S. J.; Bae, Y. C. *J. Chem. Phys.* **2014**, *141*, 064303.
- (35) Kennedy, M. R.; McDonald, A. R.; DePrince, A. E., III; Marshall, M. S.; Podeszwa, R.; Sherrill, C. D. *J. Chem. Phys.* **2014**, *140*, 121104.
- (36) Tkatchenko, A.; Alfé, D.; Kim, K. S. *J. Chem. Theory Comput.* **2012**, *8*, 4317–4322.
- (37) Bereau, T.; von Lilienfeld, O. A. *J. Chem. Phys.* **2014**, *141*, 034101.
- (38) Tainter, C.; Pieniazek, P.; Lin, Y.-S.; Skinner, J. J. *J. Chem. Phys.* **2011**, *134*, 184501.
- (39) Babin, V.; Medders, G. R.; Paesani, F. *J. Phys. Chem. Lett.* **2012**, *3*, 3765–3769.
- (40) Mas, E. M.; Bukowski, R.; Szalewicz, K. *J. Chem. Phys.* **2003**, *118*, 4404–4413.
- (41) McDaniel, J. G.; Schmidt, J. R. *J. Phys. Chem. B* **2014**, *118*, 8042–8053.
- (42) Schmidt, J.; Yu, K.; McDaniel, J. G. *Acc. Chem. Res.* **2015**, *48*, 548–556.
- (43) von Lilienfeld, O. A.; Tkatchenko, A. *J. Chem. Phys.* **2010**, *132*, 234109.
- (44) van der Hoef, M. A.; Madden, P. A. *J. Chem. Phys.* **1999**, *111*, 1520–1526.
- (45) Jakse, N.; Bomont, J.; Bretonnet, J. *J. Chem. Phys.* **2002**, *116*, 8504–8508.
- (46) Wang, L.; Sadus, R. J. *J. Chem. Phys.* **2006**, *125*, 074503.
- (47) Malijevský, A.; Malijevský, A. *Mol. Phys.* **2003**, *101*, 3335–3340.
- (48) Goharshadi, E. K.; Abbaspour, M. *J. Chem. Theory Comput.* **2006**, *2*, 920–926.
- (49) Nasrabad, A. E.; Deiters, U. K. *J. Chem. Phys.* **2003**, *119*, 947–952.
- (50) Leonhard, K.; Deiters, U. K. *Mol. Phys.* **2000**, *98*, 1603–1616.
- (51) Anta, J.; Lomba, E.; Lombardero, M. *Phys. Rev. E: Stat. Phys., Plasmas, Fluids, Relat. Interdiscip. Top.* **1997**, *55*, 2707.
- (52) Wang, L.; Sadus, R. J. *Phys. Rev. E* **2006**, *74*, 021202.
- (53) Vogt, P. S.; Liapine, R.; Kirchner, B.; Dyson, A. J.; Huber, H.; Marcelli, G.; Sadus, R. J. *Phys. Chem. Chem. Phys.* **2001**, *3*, 1297–1302.
- (54) Marcelli, G.; Sadus, R. J. *J. Chem. Phys.* **1999**, *111*, 1533–1540.
- (55) Ustinov, E. A. *J. Chem. Phys.* **2010**, *132*, 194703.
- (56) Allen, M. P.; Tildesley, D. J. *Computer Simulation of Liquids*; Clarendon Press: Oxford, 1987.
- (57) Wang, F.; Landau, D. P. *Phys. Rev. E: Stat. Phys., Plasmas, Fluids, Relat. Interdiscip. Top.* **2001**, *64*, 056101.
- (58) Wang, F.; Landau, D. *Phys. Rev. Lett.* **2001**, *86*, 2050–2053.
- (59) Desgranges, C.; Delhommelle, J. *J. Chem. Phys.* **2012**, *136*, 184107.
- (60) Shell, M. S.; Debenedetti, P. G.; Panagiotopoulos, A. Z. *Phys. Rev. E: Stat. Phys., Plasmas, Fluids, Relat. Interdiscip. Top.* **2002**, *66*, 056703.
- (61) Yan, Q.; Faller, R.; de Pablo, J. J. *J. Chem. Phys.* **2002**, *116*, 8745–8750.
- (62) Ganzenmüller, G.; Camp, P. J. *J. Chem. Phys.* **2007**, *127*, 154504.
- (63) Desgranges, C.; Delhommelle, J. *J. Chem. Phys.* **2009**, *130*, 244109.
- (64) Desgranges, C.; Delhommelle, J. *J. Chem. Phys.* **2012**, *136*, 184108.
- (65) Desgranges, C.; Delhommelle, J. *J. Chem. Phys.* **2014**, *140*, 104109.
- (66) Nasrabad, A. E.; Laghaei, R.; Deiters, U. *J. Chem. Phys.* **2004**, *121*, 6423–6434.
- (67) Cybulski, S. M.; Toczyłowski, R. R. *J. Chem. Phys.* **1999**, *111*, 10520–10528.
- (68) Korona, T.; Williams, H. L.; Bukowski, R.; Jeziorski, B.; Szalewicz, K. *J. Chem. Phys.* **1997**, *106*, 5109–5122.
- (69) Tang, K.; Toennies, J. P. *J. Chem. Phys.* **1984**, *80*, 3726–3741.
- (70) Gobre, V. V.; Tkatchenko, A. *Nat. Commun.* **2013**, *4*, 2341.
- (71) Tkatchenko, A. *Adv. Funct. Mater.* **2015**, *25*, 2054–2061.
- (72) Desgranges, C.; Kastl, E. A.; Aleksandrov, T.; Delhommelle, J. *Mol. Simul.* **2010**, *36*, 544–551.
- (73) Aleksandrov, T.; Desgranges, C.; Delhommelle, J. *Fluid Phase Equilib.* **2010**, *287*, 79–83.
- (74) Aleksandrov, T.; Desgranges, C.; Delhommelle, J. *Mol. Simul.* **2012**, *38*, 1265–1270.
- (75) Desgranges, C.; Hicks, J. M.; Magness, A.; Delhommelle, J. *Mol. Phys.* **2010**, *108*, 151–158.
- (76) Ngale, K. N.; Desgranges, C.; Delhommelle, J. *Mol. Simul.* **2012**, *38*, 653–658.
- (77) Desgranges, C.; Ngale, K.; Delhommelle, J. *Fluid Phase Equilib.* **2012**, *322–323*, 92–96.
- (78) Hicks, E. A.; Desgranges, C.; Delhommelle, J. *Mol. Simul.* **2014**, *40*, 656–663.
- (79) Lyubartsev, A. P.; Martsinovski, A. A.; Shevkunov, S. V.; Vorontsov-Velyaminov, P. N. *J. Chem. Phys.* **1992**, *96*, 1776–1783.
- (80) Escobedo, F.; de Pablo, J. J. *J. Chem. Phys.* **1996**, *105*, 4391.
- (81) Muller, M.; Paul, W. *J. Chem. Phys.* **1994**, *100*, 719–724.
- (82) Singh, J. K.; Errington, J. R. *J. Phys. Chem. B* **2006**, *110*, 1369–1376.
- (83) Escobedo, F. A.; Martinez-Veracoechea, F. J. *J. Chem. Phys.* **2008**, *129*, 154107.
- (84) Shi, W.; Maginn, E. J. *J. Chem. Theory Comput.* **2007**, *3*, 1451–1463.
- (85) Rane, K. S.; Murali, S.; Errington, J. R. *J. Chem. Theory Comput.* **2013**, *9*, 2552–2566.
- (86) Desgranges, C.; Delhommelle, J. *J. Phys. Chem. B* **2014**, *118*, 3175.
- (87) Gelb, L. D.; Gubbins, K.; Radhakrishnan, R.; Sliwinski-Bartkowiak, M. *Rep. Prog. Phys.* **1999**, *62*, 1573.
- (88) Steele, W. A. *Surf. Sci.* **1973**, *36*, 317–352.
- (89) Porcheron, F.; Rousseau, B.; Fuchs, A. H.; Schoen, M. *Phys. Chem. Chem. Phys.* **1999**, *1*, 4083–4090.
- (90) Padilla, P.; Toxvaerd, S. *J. Chem. Phys.* **1994**, *101*, 1490.
- (91) Delhommelle, J.; Millie, P. *Mol. Phys.* **2001**, *99*, 619–625.
- (92) Vargaftik, N. B.; Vinogradov, Y. K.; Yargin, V. S. *Handbook of Physical Properties of Liquids and Gases*; Begell House: New York, 1996.
- (93) Myers, A. L.; Monson, P. A. *Langmuir* **2002**, *18*, 10261–10273.
- (94) Hicks, J. M.; Desgranges, C.; Delhommelle, J. *J. Phys. Chem. C* **2012**, *116*, 22938–22946.
- (95) Koenig, A. R. V.; Desgranges, C.; Delhommelle, J. *Mol. Simul.* **2014**, *40*, 71–79.